Optimization of path-integral tensor-multiplication schemes for open quantum systems

L. M. J. Hall¹,* A. Gisdakis², and E. A. Muljarov^{1†}

¹School of Physics and Astronomy, Cardiff University, Cardiff CF24 3AA, United Kingdom,

²School of Physics and Astronomy, University of Birmingham,

Edgbaston, Birmingham B15 2TT, United Kingdom

(Dated: August 25, 2025)

Path-integral techniques are a powerful tool used in open quantum systems to provide an exact solution for the non-Markovian dynamics. However, the exponential scaling of the tensor size with quantum memory length of these techniques limits the applicability when applied to systems with long memory times. Here we provide a general optimization of tensor multiplication schemes for systems with pair correlations and finite memory times. This optimization effectively reduces the tensor sizes by using a matrix representation of tensors combined with singular value decomposition to filter out negligible contributions. This approach dramatically reduces both computational time and memory usage of the traditional tensor-multiplication schemes. Calculations that would require over 50 million GB of RAM in the original approach are now available on standard computers, allowing access to new regimes and more complex systems. While more memory-efficient representations exist, this approach enables an extrapolation scheme that other techniques do not offer. As a demonstration, we apply it to the Trotter decomposition with linked cluster expansion technique, and use it to investigate a quantum dot-microcavity system at larger coupling strengths than previously achieved. We also apply the optimization in a case where the memory time is very long – specifically in a system containing two spatially separated quantum dots in a common phonon bath.

I. INTRODUCTION

Decoherence phenomena and energy relaxation dynamics of open quantum systems are characterized by the interaction between the system and its surrounding environment (the bath). In the simplest case of a weak interaction with the environment, it can be assumed that the bath lacks memory (i.e., is Markovian) and remains uncorrelated with the system. This assumption allows the use of Born and Markov approximations [1-3] resulting in time-local equations of motion. This is also valid if the effect of the environment on the system occurs on a much larger timescale than the correlation time of the environment. However, many quantum systems deviate from this idealized case, where memory effects play a critical role and render the Born-Markov approximation invalid. In such non-Markovian regimes, the system's evolution depends on its past interactions, leading to complex phenomena [4–7]. Accurately capturing these non-Markovian effects is essential but comes with significant computational challenges, often limiting the scope of treatable systems and coupling regimes.

The typical approaches to solving the dynamics in non-Markovian open quantum systems can be divided into approximate and numerically-exact methods. For example, in a quantum dot (QD)-cavity system coupled to a bath of acoustic phonons, the approximate treatments are typically limited to specific parameter regimes, such as strong QD-cavity coupling and weak electron-phonon interaction [8], and may be improved by perturbative

and variational approaches to the phonons [9]. However, for stronger electron-phonon interaction, phonons play a more significant role that may require treating the system in a numerically exact way [10, 11].

In contrast, numerically exact techniques, such as Feynman's path integral formulation, are very well suited for system-bath dynamics as they avoid dealing with the large Hilbert space of the bath by targeting the system's reduced density matrix. The formulation takes into account the effects of a harmonic bath on the system dynamics through the well known Feynman-Vernon influence functional [12], valid for any system-bath coupling strength. In practice, the issue is that the influence functional is nonlocal in time, meaning that the coordinates of a path at any particular time point are connected to those at all other time points, leading to full temporal entanglement. As a result, the number of correlations that must be accounted for grows with each time step, leading to an exponential scaling with propagation time and thus restricting simulations to short timescales. However, it is known that these nonlocal correlations decay over time, and the influence functional operates within a finite time interval called the memory time. This fact forms the basis which resulted in the development of the iterative quasi-adiabatic propagator path integral approach (i-QuAPI), which exploits the finite memory time to evaluate the dynamics of the reduced density matrix for an arbitrary time length, not limited to only short times [13– 18]. By combining Trotter's decomposition [19, 20] with the finite memory time, the latter is discretized into a finite number of time steps, and only the information at each of the time points due to the discretization must be stored to simulate the quantum dynamics. The number of these time steps within the memory time is commonly referred to as the number of neighbors L [21] determin-

^{*} Luke.Hall415@gmail.com

[†] Egor.Muljarov@astro.cf.ac.uk

ing the number of correlations which form the influence functional. Thus, the finite memory time results in an influence functional of a fixed size, leading to linear scaling of the computational time with the number of propagations. However, the memory storage requirements can quickly become too large if one wishes to have a finer discretization, and in some systems convergence is not achievable. To address this, filtering techniques [22–24], modified truncation schemes [25], and in some regimes blip decomposition [26, 27] have been developed to offer improvements to the storage requirements or extend the applicability of the existing path-integral schemes to longer memory times. However, there is still great difficulty in accurately modeling systems where memory effects from the environment are significant, such as energy transfer processes with long coherence times (e.g., photosynthetic complexes) or multi-qubit decoherence in structured environments [28, 29].

There are various other path-integral approaches which all exploit the finite memory time of the bath in an attempt to simulate the quantum dynamics [21, 30–32]. Of recent interest, an approach utilizing modern tensor network (TN) techniques called the time-evolving matrix product operator (TEMPO) algorithm [33] (later packaged as OQuPY [34]) has provided exceptional reductions in memory requirements. Several other works build on the TEMPO algorithm, such as including an off-diagonal system bath coupling to the Hamiltonian, leading to multi-time correlations [35]. Or refinements exploiting the symmetries of the influence functional, improving efficiency of the numerical simulations [36, 37]. However, while TEMPO can achieve large values of neighbors L, the singular value decomposition (SVD) threshold must be decreased as L increases, to ensure an accurate calculation, which in turn increases computational resource demands. An automated compression of environments (ACE) algorithm [38] is another tensor network approach, similar to TEMPO, which further reduces requirements by concentrating only on the most relevant degrees of freedom of the bath.

In this work, we focus on one of the aforementioned, numerically exact tensor multiplication scheme, developed in parallel with TEMPO, which is the Trotter decomposition technique with linked cluster expansion [21]. This method has already been applied to various systems and calculations of several observables or elements of the reduced density matrix, such as four-wave mixing polarization in QD-cavity systems [39], linear polarization in multi-qubit systems [29], and population dynamics in Förster coupled QDs [40]. However, being a tensor multiplication scheme, it also suffers from the exponential scaling with time steps included in the finite memory time.

In this paper, we develop an intuitive optimization scheme to the propagator and influence functional tensors used in a general path-integral based tensor multiplication approach with pair correlations and finite memory time. For demonstration, we use the Trotter decomposition technique with linked cluster expansion as a reliable tool for calculation of the exact quantum dynamics of an open quantum system. To ease the presentation, we introduce the optimization scheme first in a simpler case of a linear optical response of a QD-cavity system treated in [21], allowing us to clearly demonstrate and intuitively explain the optimization scheme, and then generalize it to more complex situations.

The optimization is applicable to systems of any basis size and to any elements of the reduced density matrix, and has already been used for calculation of the population dynamics in Förster coupled QDs [40]. The optimization reduces the influence functional tensor sizes by remapping them to normal matrices and utilizes SVD to filter out negligible contributions, in this way reducing storage requirements and computational time. Furthermore, we express the propagator tensor as a product of exponentials each describing pair correlations and provide an efficient way to propagate the system without storing the tensor at all. The reduction in storage requirements results in approximately twice the maximum number of neighbors L (discrete time steps in the influence functional) included than previously available. This provides better accuracy in systems with longer memory times and access to new parameter regimes. For reference, to achieve the new level of accuracy using the original method, it would require over 50 million GB of RAM. but now this is available on a standard PC.

The main conceptual difference of our optimization scheme compared to other approaches, e.g. [33–38], is that we do not employ TN techniques. The TN representation directly provides the first level of optimization in terms of memory requirements, but consequently introduces many extra degrees of freedom and links which need to be controlled and optimized further. This can lead to some difficulties determining convergence and also largely incorrect results in some cases if not careful with the chosen parameters. Although TNs provide a more memory-efficient representation for the tensors, this approach enables the usage of an extrapolation scheme not presently available in other techniques [34]. The extrapolation procedure accurately approximates the exact $(L \to \infty)$ long-time dynamics which requires sufficient data generated by the optimization scheme. Furthermore, in cases where calculations are already well converged using the original tensor-multiplication scheme, the optimization provides substantial time savings, often improving efficiency by two orders of magnitude.

The paper is organized as follows: Sec. II outlines the general class of systems to which the optimization is directly applicable, and which systems we choose in this paper for illustration. Sec. III summarizes the path-integral formulation for the Trotter decomposition with linked cluster expansion technique, on which the optimization scheme is illustrated. Sec. IV introduces the optimization itself on the simplest example of a 2×2 reduced density matrix, then generalizes it to an arbitrary number of quantum states. Sec. V verifies the optimization scheme

by comparing the optimized calculation with calculations via the original technique and the TEMPO algorithm. Sec. VI discusses the extrapolation method which allows us to accurately approximate the exact (infinite neighbors) calculation.

Sec. VII is devoted to new physical results. Firstly, we use the optimization scheme to investigate the dephasing rates in a QD-cavity system interacting with acoustic phonons in the regime of very strong exciton-cavity coupling, not yet explored in the literature by any numerically exact methods. We show in particular that in this regime, the decoherence of the system in dominated by virtual phonon-assisted transitions. Secondly, we show the necessity of the optimization scheme in systems with very long memory times, using for illustration a system of two spatially separated QDs inside a microcavity, in which QD excitons interact to a common phonon bath. When the system has a long memory time, the discretization and subsequent time steps within the memory time may be too long to accurately model the quantum dynamics. Thus, by applying the optimization, we gain a finer discretization of memory time and achieve convergence.

II. SYSTEM HAMILTONIAN

The optimization presented in this paper can be applied to any number of two-level systems (TLSs) that are directly coupled and interact with an environment, either a shared one or independent baths. Additionally, they may interact with an arbitrary number of photonic cavities.

The general form of the Hamiltonian that is treatable is (in units of $\hbar = 1$)

$$H = H_0 + H_{\rm IB} \,, \tag{1}$$

where H_0 describes both the coupling between the TLSs and the TLS-cavity couplings, and is given by

$$H_0 = \sum_{ij} H_{ij} d_i^{\dagger} d_j + \sum_k \Omega_{C,k} a_k^{\dagger} a_k + \sum_{jk} g_{jk} \left(d_j^{\dagger} a_k + a_k^{\dagger} d_j \right). \tag{2}$$

Here, H_{ij} are the matrix elements of the coupled TLSs, with the diagonal elements (H_{jj}) corresponding to the excitation energy of the TLS at site j, while the off-diagonal elements $(H_{ij}, \text{ for } i \neq j)$ describe the direct coupling between TLSs at sites i and j. The fermionic operator d_j^{\dagger} creates an excitation in the two-level system at site j, and a photon in a cavity mode k has energy $\Omega_{C,k}$ and is created by the bosonic operator a_k^{\dagger} . Finally, the TLS at site j is coupled to a cavity mode k with strength g_{jk} . In general, there can be multiple baths of 3D bosons, described by

$$H_{\rm B} = \sum_{l} \sum_{\mathbf{q}} \omega_{q,l} b_{\mathbf{q},l}^{\dagger} b_{\mathbf{q},l} , \qquad (3)$$

where $b_{\mathbf{q},l}^{\dagger}$ creates an excitation in bath l with wave vector \mathbf{q} . Within Eq. (1), $H_{\mathrm{IB}} = H_{\mathrm{B}} + H_{\mathrm{int}}$ is a generalization of the independent boson model [41], consisting of the free-phonon Hamiltonian H_{B} and the TLS-bath interaction

$$H_{\text{int}} = \sum_{j} d_{j}^{\dagger} d_{j} \sum_{l} \sum_{\mathbf{q}} \lambda_{\mathbf{q},jl} (b_{\mathbf{q},l} + b_{-\mathbf{q},l}^{\dagger}), \qquad (4)$$

where $\lambda_{\mathbf{q},jl}$ describes the interaction strength of the TLS at site j with bath mode \mathbf{q} in bath l. In particular, Eq. (4) can be used to describe the scenarios where multiple TLSs are coupled to the same bath or coupled to their own independent baths. The diagonal TLS-bath coupling is needed for an exact solvability of the independent-boson Hamiltonian H_{IB} via linked cluster expansion. However, it has been recently shown that the path-integral based approaches can also be efficiently used for non-diagonal coupling [35].

By choosing the number of TLSs and turning on/off specific coupling terms, this general model given by Eqs. (1)–(4) can be reduced to describe many physical systems, such as energy transport in biological systems [42, 43], qubits in microwave resonators [44, 45], quantum dots interacting with a micromechanical resonator [46], spin-qubit systems [47], and so on.

The specific implementation of the TLSs considered in this paper are semiconductor QDs which are coupled to an environment modeled as a bath of acoustic phonons. Although the general Hamiltonian detailed above describes the range of problems this optimization can treat but is not limited to, we reduce this Hamiltonian to two cases used for illustration. Case 1: a QD-cavity system coupled to a bath of acoustic phonons detailed in [21]: Case 2: a QD-QD-cavity system coupled to the same phonon bath, detailed in [29]. Importantly, in Case 2, the long memory times are due to the shared bath, where phonons may travel between the QDs. So, the memory time can be as long as the phonon coherence time, and the larger the dot separation, the larger the memory time, which manifests itself as a delay in the bath correlation functions. For ease of reference, the Hamiltonians for both cases are provided in Appendix A, and details of the exciton-phonon coupling elements and phonon spectral density for these systems are given in Appendix B.

III. PATH-INTEGRAL APPROACH

For illustration we consider the linear optical response, which we call the linear polarization, as a simple quantum correlator to investigate. However any element of the density matrix, and other quantum correlators may be treated in a similar way, such as the FWM polarization [39] or populations [40]. The linear optical polarization is given by $P_{jk}(t) = \text{Tr}\{\rho(t)d_j\}$ by definition, where k and j denote, respectively, the excitation channel at t=0 and measurement channel at the observation time t, and $\rho(t)$ is the full density matrix. As has been derived in

Ref. [21], the linear polarization can be written as

$$P_{jk}(t) = \langle \langle j | \hat{U}(t) | k \rangle \rangle_{B}, \qquad (5)$$

where $\hat{U}(t) = e^{iH_{\rm B}t}e^{-iHt}$ is the evolution operator and $\langle ... \rangle_{\rm B}$ denotes the expectation value over all phonon degrees of freedom in thermal equilibrium. Common to path-integral based approaches, the time interval [0,t], where t is the observation time, is split into N equal steps of duration $\Delta t = t/N = t_n - t_{n-1}$, where $t_n = n\Delta t$ represents the time at the n-th step. Trotter's theorem is then used to separate the time evolution of the two non-commuting components of the Hamiltonian, H_0 and $H_{\rm IB}$. In fact, applying Trotter's decomposition theorem, the time evolution operator $\hat{U}(t)$ can be written as

$$\hat{U}(t) = \lim_{\Delta t \to 0} e^{iH_{\rm B}t} (e^{-iH_{\rm IB}\Delta t} e^{-iH_0\Delta t})^N.$$
 (6)

The final exponential in Eq. (6) describes the dynamics of the system in the absence of phonons and is written as an operator \hat{M} :

$$\hat{M}(t_n - t_{n-1}) = \hat{M}(\Delta t) = e^{-iH_0\Delta t}.$$
 (7)

However, the necessity of the path-integral approach arises due to the interaction of the system with the bath within $H_{\rm IB}$ which can be handled in various ways but always results in a tensor multiplication scheme of some form, which the present optimization scheme can be used for. In particular, we choose to apply linked cluster expansion [41]. This leads to the tensor multiplication scheme used in [21, 29, 39, 40]:

$$F_{pi_L...i_2}^{(s+1)} = \sum_{i_1} \mathcal{G}_{pi_L...i_1} F_{i_L...i_1}^{(s)}, \qquad (8)$$

where \mathcal{G} is known as the propagator and $F^{(s)}$ as the full influence functional, and Fig. 1 shows the path segments contained in the tensors. Key details of the approach are outlined in Appendix C. The role of \mathcal{G} is to propagate the system forward in time, taking the tensor $F^{(s)}$ to $F^{(s+1)}$, where F contains all correlations within the memory time. In particular, F captures how past states influence the present dynamics, incorporating non-Markovian effects. The number of correlations, or time steps, included in the F tensor is also referred to as the number of neighbors, L, with Fig. 1 depicting 4 neighbors. Each index i_n of the tensor can have J possible values, corresponding to J different quantum states within the reduced density matrix. For example, in Case 2 of a QD-QD-cavity system, J=3, where we define $i_n=1$ or $i_n = 2$ to correspond to the excitonic channels in QD 1 or 2, respectively, and $i_n = 0$ represents the cavity channel. At any time step n within the memory kernel, the excitation can transfer between these components, meaning that the index i_n within the tensors must account for the fact that the system oscillates between QD 1, QD 2, and the cavity.

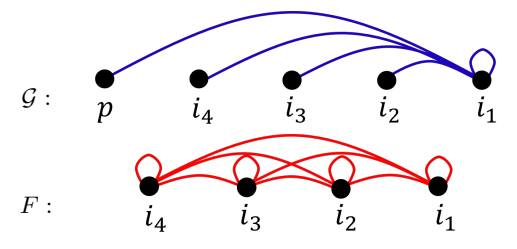


FIG. 1. Diagrams showing the path segments contained within \mathcal{G} (blue) and F (red) for L=4. The propagator \mathcal{G} contains path segments connecting the given time (indexed by i_1) to itself and to all other considered nearest time intervals (neighbors, indexed by i_n). Each link is weighted appropriately, forming a memory kernel. The full influence functional F represents the information about the state of the system and contains all considered path segments and all possible links between them.

In Fig. 1, \mathcal{G} shows a specific case of two-time correlations, employed in all of the path-integral techniques mentioned so far. This is a consequence of the assumption that the system-bath coupling is bilinear in system operators (and linear in the bath operators), in which case all higher-order correlation functions can be expressed in terms of the two-time correlations. In the present case of the exactly solvable IB model describing the system-bath interaction, the cumulant expansion gives the exact result in its lowest (second) order, so \mathcal{G} is given by

$$\mathcal{G}_{p\dots i_1} = M_{i_2 i_1} e^{\mathcal{K}_{i_1 i_1}(0) + 2\mathcal{K}_{i_2 i_1}(1) + 2\mathcal{K}_{i_3 i_1}(2) + \dots + 2\mathcal{K}_{p i_1}(L)},$$
(9)

where K denotes a cumulant arising from the application of linked cluster expansion [41]. The cumulants contain two indices, i_n and i_m , describing correlations between two time points t_n and t_m , and take into account the fact that not all components of the system couple to phonons. More details on the linked cluster expansion and explicit form of the cumulants can be found in Appendix C, with full details provided in Refs. [21, 29].

The initial full influence functional at the first time step is simply given by $F_{i_L...i_1}^{(1)} = M_{i_1k}$, where k is the excitation channel and M_{ij} are the matrix elements of the operator \hat{M} defined in Eq. (7). The final full influence functional $F_{i_L...i_1}^{(N)}$ at the observation time $t = N\Delta t$ is found by applying the propagator N-1 times, according to Eq. (8), and in general determines the full reduced density matrix of the system at time t. The off-diagonal elements of this density matrix yield the linear optical polarization, which is given by

$$P_{jk}(t) = e^{\mathcal{K}_{jj}(0)} F_{0...0j}^{(N)}. \tag{10}$$

Here, the subscripts 0...0 represent the indices placed into the cavity channel, which is not coupled to phonons, but more generally, this can be any channel decoupled from the bath, such as the absolute ground state of the system.

As the number of time steps within the memory kernel increases (increasing neighbors), the tensors in Eq. (8) are growing exponentially in size. The exponential growth limits the number of correlations that can be considered, due to computational limitations. As a consequence there are problems in achieving convergence for the following scenarios: (i) When the system has long phonon memory times; (ii) when there is a large number J of quantum states or channels; (iii) in strong coupling regimes where the quantum dynamics of the system exhibits rapid oscillations.

IV. OPTIMIZATION SCHEME

For clarity of presentation, we first introduce in Sec. IV A the optimization scheme for Case 1, which is the linear polarization in a QD-cavity system, with the QD exciton (the excited state of the TLS) coupled to a bath of acoustic phonons. This is the simplest possible non-trivial system treated by the Trotter decomposition method with cumulant expansion [21], which requires two basis states (J=2) such that $i_n=0$ $(i_n=1)$ indicates the system is in the cavity (exciton) state at time step n. While we present below the optimization for an arbitrary number of neighbors L within the so-called L-neighbor approach, all the figures in Sec. IVA use only L=4neighbors as a simpler example to ease understanding. A generalization of the optimization scheme for an arbitrary number J of basis states or elements of the density matrix is discussed in Sec. IV B.

A. Optimization for the smallest reduced density matrix, J=2

The core principle of the optimization scheme is to map the tensors in Eq. (8), in particular the full influence functional F, into two matrices and then to SVD these matrices at each time step, in order to minimize their size by filtering out contributions below a desired threshold value.

Let us consider the first time step, after excitation in channel k at t = 0. In this case, the full influence functional tensor can be fully populated by M_{i_1k} , given by Eq. (7) and then mapped onto a matrix \mathcal{F}_{nm} :

$$F_{i_1...i_1}^{(1)} = M_{i_1k} = \mathcal{F}_{nm}^{(1)}. \tag{11}$$

The full influence functional is populated by only two values of M_{i_1k} : M_{0k} or M_{1k} . In fact, following the excitation at t=0 in channel k, one further time step introduces index i_1 , which has two possible paths of evolution, $i_1=0$ and $i_1=1$. However, the tensor $F_{i_L...i_1}^{(1)}$ depends on L indices $i_L...i_1$, and consequently the matrix $\mathcal{F}_{nm}^{(1)}$ also contains the information about all of them in some form, as detailed below. This is already different from other methods, such as Ref. [33], in which there

		$(i_2, i_1) \longrightarrow$			
		00	01	10	11
(i_4, i_3)	00	M_{0k}	M_{1k}	M_{0k}	M_{1k}
	01	M_{0k}	M_{1k}	M_{0k}	M_{1k}
	10	M_{0k}	M_{1k}	M_{0k}	M_{1k}
	11	M_{0k}	M_{1k}	M_{0k}	M_{1k}

FIG. 2. The tensor $F_{i_4i_3i_2i_1}^{(1)}$ mapped onto a matrix $\mathcal{F}_{nm}^{(1)}$, with the column index corresponding to the possible values of (i_2, i_1) and the row index to (i_4, i_3) .

is always a growth phase in the early times, where each new time step introduces a new index to the tensor, up until the full memory kernel has been formed, and beyond this point the tensor has a fixed maximum number of indices. We begin instead with the full-rank tensor as a placeholder for subsequent propagation.

Fig. 2 depicts the L = 4 influence functional Fremapped to a matrix \mathcal{F}_{nm} . In \mathcal{F}_{nm} , the columns take into consideration the possible values of the indices $i_{\frac{L}{2}} \dots i_1$, and the rows add the remaining indices $i_L \dots i_{\frac{L}{2}+1}$. Note that in general L does not need to be even, but below we assume that it is even for clarity of presentation. Since the linear polarization in the QDcavity system only has the possible index options $i_n = 0$ or 1, for L/2 indices associated with each of the two matrices, there are $2^{L/2}$ index configurations to take into account. We generate all possible index configurations by enumerating all tuples $(i_{\frac{L}{2}}, \ldots, i_1)$, where each index i_n independently takes values 0 or 1. Each configuration represents a possible path of the system as it evolves over the time steps. For L=4, the configurations for each pair of indices i_2i_1 and i_4i_3 are simply $\{00,01,10,11\}$. Thus, the dimensions of the mapped matrix \mathcal{F}_{nm} are n_{max} and m_{max} , where $n_{\text{max}} = m_{\text{max}} = 2^{L/2}$ in general. However, \mathcal{F}_{nm} contains the same number of elements as the original tensor F, and therefore presently provides no memory storage reduction. To remedy this, in order to avoid constructing large tensors in the first instance, $\mathcal{F}_{nm}^{(1)}$ can be analytically expressed in SVD form. In general, this is always possible to do, and is given by

$$\mathcal{F}_{nm}^{(1)} = U_{n0} \,\Lambda_0 \,V_{0m} \,, \tag{12}$$

with $U_{n0}=1$, $\Lambda_0=1$ and $V_{0m}=M_{i_1k}$. Here Λ is the 1×1 identity matrix, but it later grows in size and is used for filtering out unimportant contributions after performing a SVD. As an example, Fig. 3 shows the matrix $\mathcal{F}_{nm}^{(1)}$ in such an SVD form for L=4. This reduces the total number of elements from 2^L to $2^{L/2+1}$, having a significant impact at larger L, approximately doubling the amount of neighbors achievable. As the matrix has now been represented in SVD form, we define a column vector U which takes into account the indices $i_L \dots i_{\frac{L}{2}+1}$ and the row vector V, taking into account indices $i_{\frac{L}{2}} \dots i_1$.

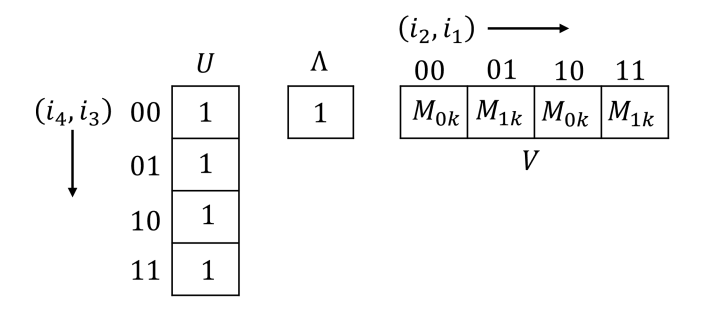


FIG. 3. The matrix in Fig. 2, $\mathcal{F}_{nm}^{(1)}$, expressed in SVD form.

For further time steps, the exciton-phonon coupling has to be considered, which is taken into account via the propagator \mathcal{G} in Eq. (8). \mathcal{G} is successively applied to propagate the system forward in time, summing over the first index, i_1 , as seen in Eq. (8). Although the propagator Eq. (9) is in the form of a tensor, the two-time correlations can be expressed as 2×2 matrices in the following way

$$Q_{pi_1}^{(L)} = \exp\left\{2\mathcal{K}_{pi_1}(L)\right\} ,$$

$$Q_{i_r i_1}^{(r-1)} = \exp\left\{2\mathcal{K}_{i_r i_1}(r-1)\right\} \quad \text{for } 2 < r \leqslant L ,$$

$$Q_{i_1 i_1}^{(1)} = M_{i_2 i_1} \exp\left\{\mathcal{K}_{i_1 i_1}(0) + 2\mathcal{K}_{i_2 i_1}(1)\right\} , \qquad (13)$$

where the superscript denotes the time step difference between any index (not including i_1) in the memory kernel and i_1 , i.e. the time step difference between the indices within each pair correlation. For example, considering the indices i_3 and i_1 , the correlations are between time points t_3 and t_1 in the memory kernel, thus the Q matrix describing these correlations is given by $Q_{i_3i_1}^{(2)}$. The recursive relation Eq. (8), can then be re-expressed as

$$F_{p\,i_{L}\dots i_{2}}^{(s+1)} = \sum_{i_{1}} Q_{p\,i_{1}}^{(L)} Q_{i_{L}i_{1}}^{(L-1)} \dots Q_{i_{3}i_{1}}^{(2)} Q_{i_{2}i_{1}}^{(1)} \mathcal{F}_{nm}^{(s)}.$$
 (14)

The product of the Q matrices must be applied to the appropriate elements of $\mathcal{F}_{nm}^{(s)}$, with a summation over index i_1 . At any time step s, $\mathcal{F}_{nm}^{(s)}$ has the SVD form

$$\mathcal{F}_{nm}^{(s)} = \sum_{k} U_{nk} \Lambda_k V_{km} \tag{15}$$

by construction, as it is clear from the following, which includes as a special case the initial, s=1 matrix given by Eq. (12). Since the matrix U (V) takes into account the indices $i_L \dots i_{\frac{L}{2}+1}$ ($i_{\frac{L}{2}} \dots i_1$), only the Q matrices which introduce pair correlations between those indices and the index i_1 should be applied to that matrix. Additionally, matrix $Q_{pi_1}^{(L)}$ bringing in a new index p is applied to U We then obtain two new matrices,

$$\tilde{U}_{nk}^{(i_1)} = Q_{i_L i_1}^{(L-1)} \cdots Q_{i_{\frac{L}{2}+1} i_1}^{(\frac{L}{2})} U_{nk}, \qquad (16)$$

$$\tilde{V}_{k\tilde{m}}^{(i_1,p)} = Q_{pi_1}^{(L)} Q_{i_{\frac{L}{2}}i_1}^{(\frac{L}{2}-1)} \cdots Q_{i_2i_1}^{(1)} V_{km}, \qquad (17)$$

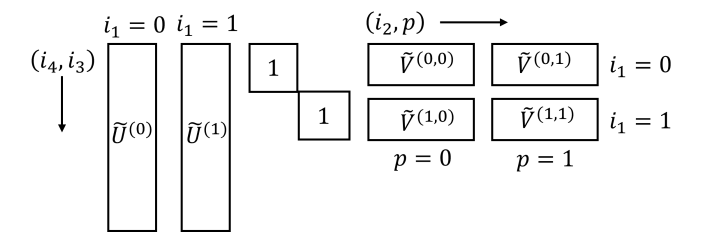


FIG. 4. The tensor $F_{p\,i_L...i_2}^{(2)}$ mapped onto a matrix $\mathcal{F}_{nm}^{(2)}$. The vectors from the initial time step, U_{n0} and V_{0m} , split through applying the Q matrices and the elements with $i_1=0$ and $i_1=1$ separated. The blocks of \tilde{V} are further split due to the extra index p, with p=0 and p=1 separated.

where the difference between m and \tilde{m} is that m includes index i_1 but \tilde{m} does not, as it is now used as a superscript in \tilde{V} . Note that as the left matrix U does not contain any information about i_1 , this index appears as an addition superscript in \tilde{U} . Similarly, the new index p in the propagator \mathcal{G} appears as another superscript in \tilde{V} , in addition to i_1 which was intentionally separated from all other indices as there is a summation over i_1 . Now, having applied all the propagator matrices, the tensor $F_{pi_1...i_2}^{(s+1)}$ in Eq. (14) remapped to a matrix given by

$$\mathcal{F}_{nm}^{(s+1)} = \sum_{i_1} \sum_{k} \tilde{U}_{nk}^{(i_1)} \Lambda_k \tilde{V}_{k\tilde{m}}^{(i_1,p)}$$
 (18)

and expressing propagation of the system forward in time, where the difference between indices m and \tilde{m} is that m now includes the new index p but \tilde{m} does not.

With reference to the L=4 special case illustrated in Fig. 3 for s=1, the propagator matrices $Q_{i_2\,i_1}^{(1)}$ and $Q_{p\,i_1}^{(4)}$ are applied to the right vector V, and matrices $Q_{i_3\,i_1}^{(2)}$ and $Q_{i_4\,i_1}^{(3)}$ to the left vector U. As there is no information about index p contained within either left or right vectors, both possibilities of p=0 and 1 must be taken into account. Fig. 4 shows the s=2 newly propagated matrix $\mathcal{F}_{nm}^{(2)}$ for L=4, where \tilde{U} and \tilde{V} have been split into blocks due to the summation over i_1 in Eq. (18), and according to Eq. (17), the Q matrices have been applied, further splitting \tilde{V} into four blocks due to the introduction of a new index p in the propagator.

In the recursion relation Eq. (8) [or Eq. (14)], $F_{pi_L...i_2}^{(s+1)}$ must become the new $F_{i_L...i_1}^{(s)}$ for the next time step, and we must therefore relabel the indices. As an example, for L=4, relabeled indices $i_4i_3\to i_3i_2$ becomes associated with \tilde{U} and $i_2p\to i_1i_4$ with \tilde{V} . In addition to this change of indices, we rename the matrices \tilde{U} and \tilde{V} back to U and V. In other words, after each time step, the blocks \tilde{U} and \tilde{V} form the new U and V, as illustrated in Fig. 5, having the same size in the dimensions associated with the new indices as the old matrices but generally different size in the other dimension, given by the indices of summation i_1 and k in Eq. (18).

Applying Eq. (14) further, in each successive time step,

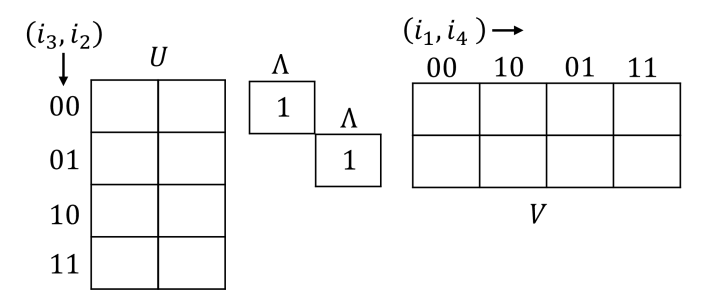


FIG. 5. The tensor $F_{i_L...i_1}^{(2)}$ mapped onto a matrix $\mathcal{F}_{nm}^{(2)}$, with matrices U and V redefined and the indices relabeled. This is the starting point of the next time step, in which the subsequent application of the Q matrices and splitting due to $i_1=0,1$ and p=0,1 will be applied again to propagate the system.

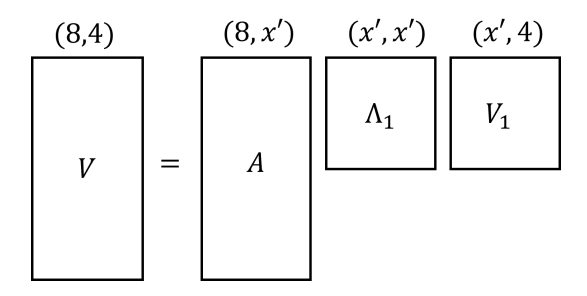


FIG. 6. SVD applied on V after the third time step (s=4), where there are now 8 rows. The number of columns (4 for L=4) is fixed due to the fixed number of configurations $2^{L/2}$ for a given number of neighbors L. By applying SVD with a threshold value, the truncated dimension becomes x'. The truncated matrix V_1 replaces V and is used for further propagation.

the indices will cycle, but once the index i_1 becomes associated with U, which occurs after L/2 steps, the original index ordering has been restored but on opposite matrices. Specifically, $i_{L/2} \dots i_1$ is now instead associated with U and $i_L \dots i_{\frac{L}{2}+1}$ with V. Once this occurs, it is computationally simpler to transpose all the matrices and redefine, such that $V^T \to U$ and $U^T \to V$, allowing us to repeat the procedure outlined in this section above.

It is clear that through the splitting due to $i_1 = 0$ and 1 after each time step, the size of U matrix doubles in size relative to the previous step, and through the splitting due to p = 0 and 1, V also doubles in size. However this can be optimized, reducing the sizes, by SVDing the matrices. For instance, we can SVD V, as shown in Fig. 6, where Λ_1 which contains the significant values has a smaller size due to the threshold condition that if $\lambda_k < \epsilon \lambda_{\max}$ then $\lambda_k = 0$, where λ_{\max} is the largest value contained in Λ_1 . Clearly, this truncation of the SVD matrices does not affect their dimensions associated with the indices $i_L \dots i_1$. The threshold value ϵ may be chosen based on the desired accuracy of the calculation, and in this paper we use $\epsilon = 10^{-8}$. As seen in Fig. 6, for illustration considering V, which is initially a 1×4 matrix at the

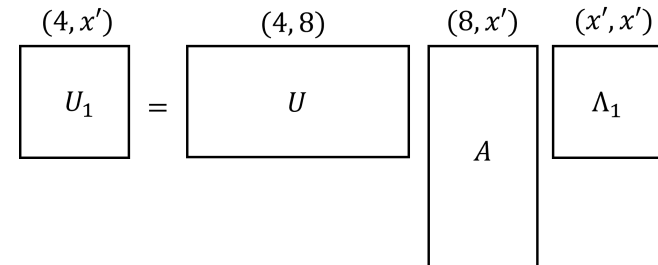


FIG. 7. The matrices A and Λ_1 from SVD of V, multiplied by U to form U_1 , which automatically truncates the dimensions without performing any further SVDs. The reduced matrix U_1 replaces U and is used for further propagation.

first time step, but has increased to an 8×4 matrix after three iterations (but would be an $8 \times 2^{L/2}$ in general, for s = 4). Then, if after applying the threshold only x' significant values remain, A is an $8 \times x'$ matrix, Λ_1 is an $x' \times x'$ matrix, and V_1 is an $x' \times 4$ matrix. Initially this appears to increase the number of required elements, however A and Λ_1 can be multiplied into U, which is a 4 × 8 matrix, and through matrix multiplication, the size of U is truncated to a matrix U_1 of size $4 \times x'$. Note that once the filtering of unimportant contributions from Λ_1 has occurred, Λ_1 can be absorbed into either U_1 or V_1 . Thus, the matrices of reduced dimension, V_1 and U_1 in Figs. 6 and 7, respectively, are used as the new V and Ufor the following time step. One can introduce an identity matrix of dimension $x' \times x'$ between the new U and V to maintain the SVD form in Eq. (15). If the truncation is insufficient after one SVD, one can apply SVD again, this time to the new matrix U, and then multiply the SVD blocks from U back into V. Effectively, there is an SVD sweeping back and forth to truncate the sizes. These truncated matrices are then used as the starting U and V for the following time step, with the SVD procedure applied every time step to prevent exponential growth of matrices.

B. Generalization to J-dimensional density matrix vectors

The procedure described in Sec. IV A for J=2 is general and computationally straightforward. It can therefore be applied to the reduced density matrix of any size, or to an arbitrary number of quantum states J describing the system. To summarize it, we start with a tensor which has a number of indices equal to the number of time steps, or neighbors, L, within the memory kernel. We then assign about a half of the indices to a matrix U, and the rest to a matrix V, with each configuration of the indices corresponding to a specific path of quantum evolution. Due to the exponential form of the propagator, it can be decomposed into matrices Q, defined in Eq. (13), which describe the correlations between two time points. The Q-matrix elements can be multiplied into U and V,

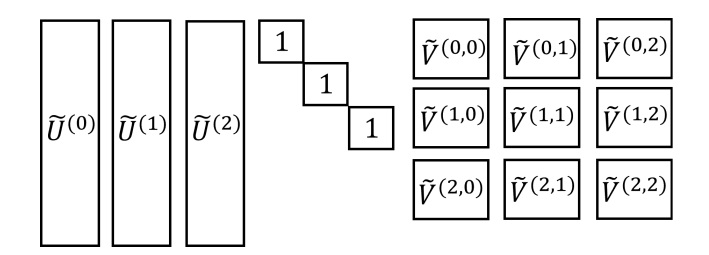


FIG. 8. As Fig. 4 but for J=3, corresponding to Case 2, the QD-QD-cavity system coupled to the phonon bath.

propagating the system. Then, via matrix multiplication of the desired rows and columns, any physical observable can be found. For example, the linear polarization in Case 1 or 2 can be found via Eq. (10). The exponential scaling of the matrix sizes (doubling at each time step for J=2) is then handled by SVDing the matrices to keep only contributions above a chosen threshold value.

Here we illustrate the more general case for a system and correlator which can be fully described by J system states, or elements of a reduced density matrix. At time step s, the tensor $F_{i_L...i_1}^{(s)}$ (where $i_n = 0, 1, ..., J-1$) is represented by a standard matrix $\mathcal{F}_{nm}^{(s)}$, which is split into two matrices U, Λ and V as before, see Eq. (15). Here Λ is simply the identity matrix for steps s=1 and s=2, but is responsible for truncation after applying SVD and filtering out unimportant contributions for any further step (s > 2). The indices are assigned to the matrices U and V, and after applying the Q matrices, blocks of \tilde{U} and \tilde{V} are formed. One main difference to the previous section dealing with J=2 is that the indices can be any of the J possible system states, rather than simply 0 or 1. Thus, the dimensions of the mapped matrix, n_{max} and $m_{\rm max}$, are dependent on J and the number of neighbors L: $n_{\rm max} = m_{\rm max} = J^{L/2}$ (for even L). In other words, there are more configurations of the indices when there are more possible system states.

The other main difference is in the number of blocks of \tilde{U} and \tilde{V} after applying the Q matrices, defined in Eq. (13). Fig. 8 shows the specific case of J=3, which may represent Case 2, the linear polarization in a QD-QD-cavity system, in which case the indices take the values $i_n=0,1,$ and 2. It illustrates the effect of the Q matrices, which are applied to the matrix elements of V and U, as described in Sec. IV A, generally resulting in J blocks of \tilde{U} and J^2 blocks of \tilde{V} , each of them being J times shorter than V.

V. VERIFICATION

Fig. 9 illustrates the accuracy of our optimization scheme by calculating the linear polarization $P_{11}(t)$ of an isotropic (spherical) QD coupled to a microcavity with coupling strength $g = 100 \,\mu\text{eV}$ and zero detuning $(\Omega_X = \Omega_C)$. We compare the results from the original

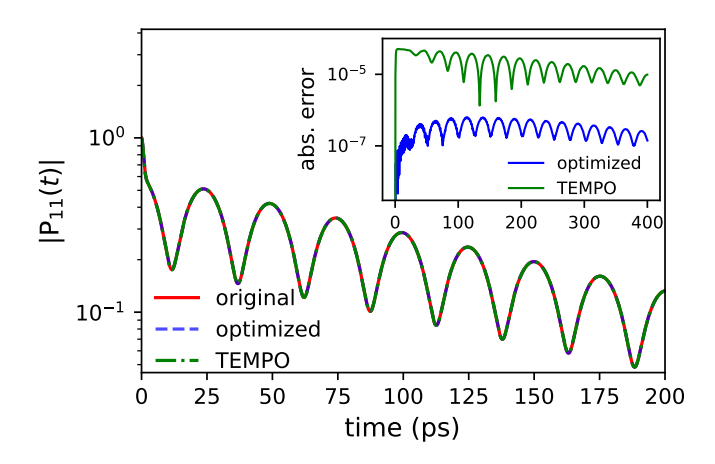


FIG. 9. Linear optical polarization $|P_{11}(t)|$ of an isotropic QD with the Gaussian confinement length $l=3.3\,\mathrm{nm}$, coupled to a microcavity with coupling strength $g=100\,\mu\mathrm{eV}$ at zero detuning, with excitation and measurement in the QD. The calculation using the original tensor multiplication scheme [21] (red) is compared with the optimized method (blue), and TEMPO (green). All calculations use the same number of neighbors, L=26, with the optimized and TEMPO methods using an SVD threshold of $\epsilon=10^{-8}$. Inset: Absolute error for the linear polarization by the optimized method and TEMPO, relative to the original calculation. The phonon bath temperature is $T=50\,\mathrm{K}$ and the acoustic phonon parameters are taken as $D_c-D_v=-6.5\,\mathrm{eV}$, where D_c (D_v) is the conduction (valence) band deformation potential, $v_s=4.6\times10^3\,\mathrm{m/s}$ is sound velocity, $\rho_m=5.65\,\mathrm{g/cm}^3$ is the mass density [48, 49].

full tensor multiplication scheme [21], the optimized calculation, and the TEMPO approach [33], using the same number of neighbors, L = 26, in each case. The same SVD threshold of $\epsilon = 10^{-8}$ is used in both the optimized and TEMPO calculations. The inset of Fig. 9 shows the absolute error in the polarization calculated using the present optimization (blue) and TEMPO (green), relative to the full original calculation, which is well converged in this case. It demonstrates a close agreement between the optimized scheme and the original full tensor method confirming the validity of the present approach, while the comparison with TEMPO serves as an additional point of reference. The observed two orders of magnitude larger error using the TEMPO method is because this technique has more matrices and therefore performs more SVDs which accumulates the SVD truncation error. This is further discussed in Sec. VI. There is a large benefit to computational time, taking roughly 1300 seconds using the original approach, compared with only 30 seconds using the optimization scheme, for the same number of neighbors. Furthermore, the memory storage requirement is over 4000 times less than the original approach for this number of neighbors. Note that the maximum achievable neighbors in the original full calculation for this QD-cavity system is L=26 for a desktop PC of 8GB RAM, whereas in the optimized case it is approximately L = 50, which would require for the original (unoptimized) method over 50 million GB of RAM.

VI. EXTRAPOLATION

As detailed in [21, 29], the strong coupling between the exciton and cavity forms a polariton, and the oscillatory behavior in Fig. 9 is explained by the coherent exchange of quantum information between the QD and the cavity. The energy levels of the polariton states (hybrid QD-cavity states) are separated by the Rabi splitting, R, which determines the beat frequency in $|P_{11}(t)|$. The temporal decay of the linear polarization expresses the decoherence in this system as a consequence of the interaction of the QD with the bath. This decoherence is due to phonon-assisted transitions between the upper $|+\rangle$ and lower $|-\rangle$ polariton states, see Sec. VII A and [29] for more details.

Using this picture, we have applied to the long-time dynamics of $P_{11}(t)$ a biexponential fit of the form

$$P_{11}^{\text{fit}}(t) = \sum_{j} C_j e^{-i\omega_j t}, \qquad (19)$$

extracting the complex amplitudes C_j , energies $\text{Re }\omega_j$, and dephasing rates $\Gamma_j = -\text{Im }\omega_j$ of the phonon-dressed polariton states. It turns out that these extracted parameters follow a power law dependence on the number of neighbors L, for sufficiently large L. Therefore, one can calculate the linear optical polarization for a given number of neighbors, apply a fit Eq. (19) to the long time data, extract the fit parameters, and then apply a power-law fit to these parameters across an accessible range of L values. The resulting parameters of this fit are used to perform a power-law extrapolation, estimating the exact value which corresponds to $L = \infty$.

As an example, consider the parameters corresponding to the dephasing rates, $\Gamma(L)$ extracted across a range of neighbors, where the convergence of $\Gamma(L)$ to the exact $(L=\infty)$ value is assumed to follow a power law model, given by

$$\Gamma(L) = \Gamma(\infty) + \alpha L^{-\beta}.$$
 (20)

Figure 10 shows the $\Gamma(L)$ calculated values (blue crosses) in the QD-cavity system, with the power law model applied (red curve), and the extrapolated $\Gamma(\infty)$ is shown as a red dashed line. The value of $\Gamma(\infty)$ is estimated for the values of $\Gamma(L)$ shown in Fig. 10 by minimising the root mean square deviation from the power law Eq. (20) for $\beta=2$. Note that we first let β be a fit parameter but found that it is always close to $\beta=2$, and therefore fixed this value. Fig. 10 also demonstrates the necessity of the extrapolation, since optimization alone may not be well converged in some cases. However, the extra data provided by the optimization by achieving more neighbors allows for an accurate usage of the extrapolation. In fact, in some systems with very long memory times, such as in spatially extended quantum systems,

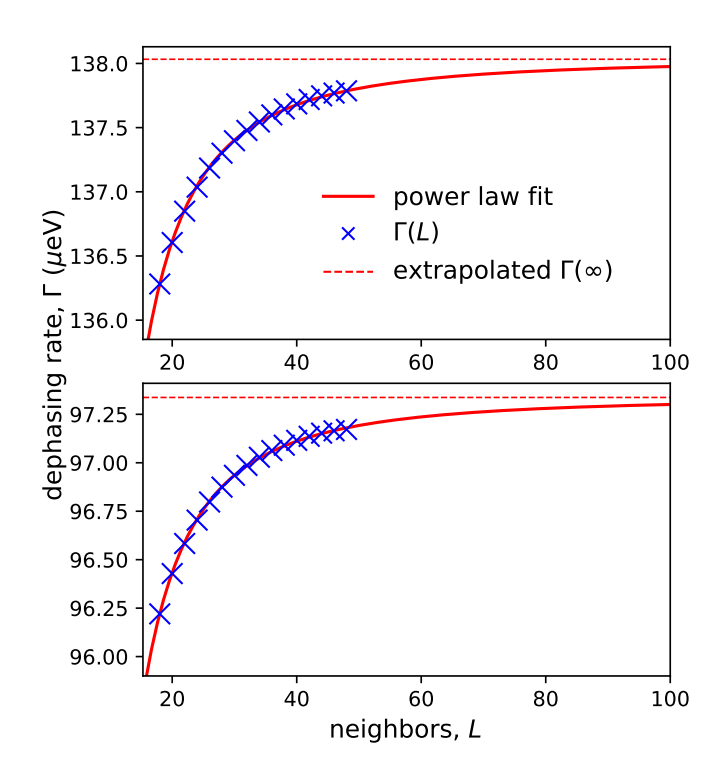


FIG. 10. Power law fit applied to $\Gamma_{+}(L)$ (upper panel) and $\Gamma_{-}(L)$ (lower panel) across the range of L values shown, for $g = 600 \,\mu\text{eV}$. The blue crosses are the values of $\Gamma_{\pm}(L)$ extracted from the biexponential fit, the red curves are the power law fit with $\beta = 2$, and the red horizontal dashed lines are the extrapolated values of $\Gamma_{\pm}(\infty)$. The rest of the parameters are as in Fig. 9.

the extrapolation is not possible at all with the original technique and requires the data from the optimization scheme. Interestingly, the extrapolation does not work in other methods. The reason for this is that the extrapolation does requires calculations across a range of neighbors, and the same SVD threshold must be used across all calculations for consistency and smooth convergence behaviour. However, in other techniques, as the number of neighbors is increased, the SVD threshold typically must be decreased, resulting in an unsmooth convergence behaviour which cannot be extrapolated. This is a consequence of the more memory efficient representations for the tensors, e.g. matrix product states in TNs [34, 38]. However, in the optimization developed in this work, only two matrices are used to represent tensors, and therefore the same number of SVD applications are used regardless of the number of neighbors. With reference to Fig. 9, despite TEMPO and the approach in this paper using the same number of neighbors, the TEMPO algorithm applies SVD to more matrices and therefore results in a larger error due to accumulated truncation error. We note that in the original paper on TEMPO [33], a smooth dependence of the decay rate on L was demonstrated; however, such features are not accessible in open source libraries, such as OQuPY [34].

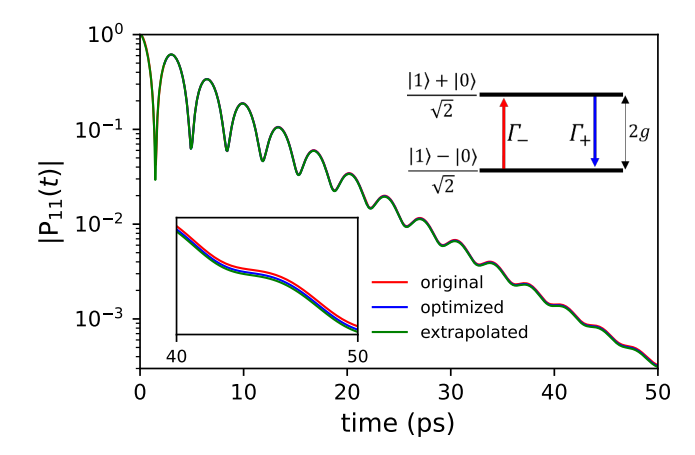


FIG. 11. Linear optical polarization $|P_{11}(t)|$ of an isotropic QD with $l=3.3\,\mathrm{nm}$, coupled to a microcavity with coupling strength $g=600\,\mu\mathrm{eV}$ at zero detuning, calculated using the original tensor multiplication scheme with L=26 (red), the optimized scheme with L=48 and SVD threshold $\epsilon=10^{-8}$ (blue), and extrapolation (green). Inset: Energy level diagram for the hybridized QD-cavity states $|\pm\rangle=(|1\rangle\pm|0\rangle)/\sqrt{2}$, with real phonon-assisted transitions (red and blue arrows). The phonon bath parameters are as in Fig. 9.

VII. RESULTS

A. Accessing stronger coupling regimes in the QD-cavity system

Fig. 11 shows the linear optical polarization $P_{11}(t)$ of an isotropic QD coupled to a microcavity with coupling strength $g=600\,\mu\text{eV}$ at zero detuning. The data is calculated with the original tensor-multiplication scheme, the optimization and extrapolation. There is good convergence of the original calculation at this coupling strength because the time step Δt , which decreases as the number of neighbors increases, is small enough to resolve the dynamics of the Rabi oscillations. The frequency of the Rabi oscillations is determined by the energy splitting between the polariton states, which is $R\approx 2g$ at zero detuning (see the right inset of Fig. 11). Therefore, as g increases, a smaller time step is required for an accurate calculation. The optimization and extrapolation thus provides access to larger coupling strengths.

Fig. 12 shows the dephasing rates Γ_{\pm} in the QD-cavity system as a function of the coupling strength g. The optimized and extrapolated data visually align with the original calculation at smaller coupling strengths, but show a deviation at larger values as expected. Provided that the parameters extracted via the optimization scheme follow the power law convergence, the extrapolated values are much more accurate for significantly larger coupling strengths than in the original approach [21]. The inset of Fig. 12 shows the extrapolated error for each of the extrapolated Γ_{\pm} values, where even at $g=3000~\mu\text{eV}$ the extrapolated error $(10^{-3}~\mu\text{eV})$ is much less than the

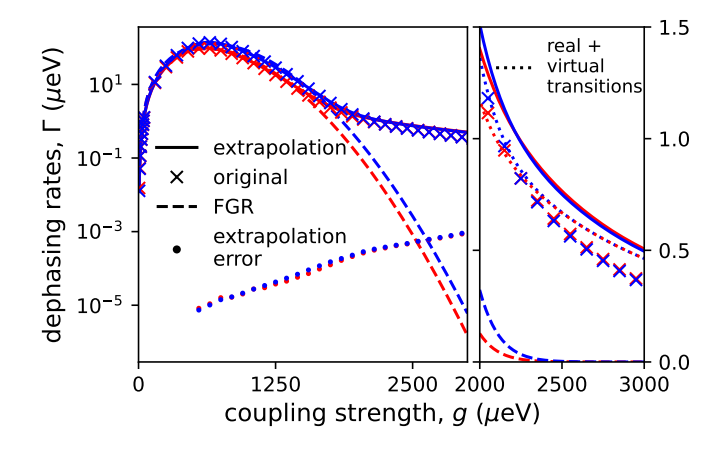
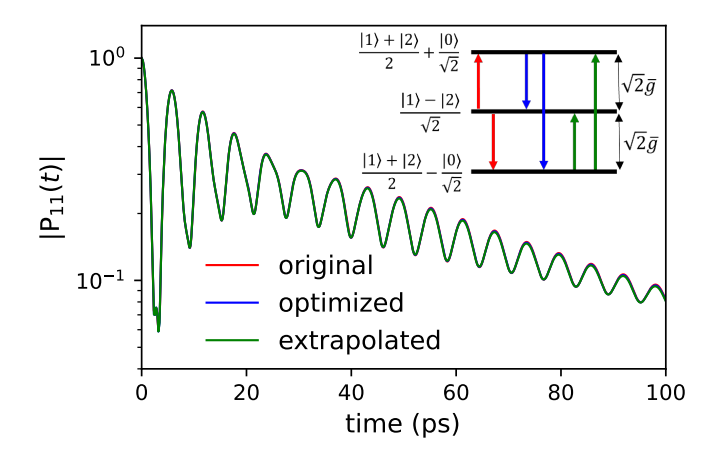
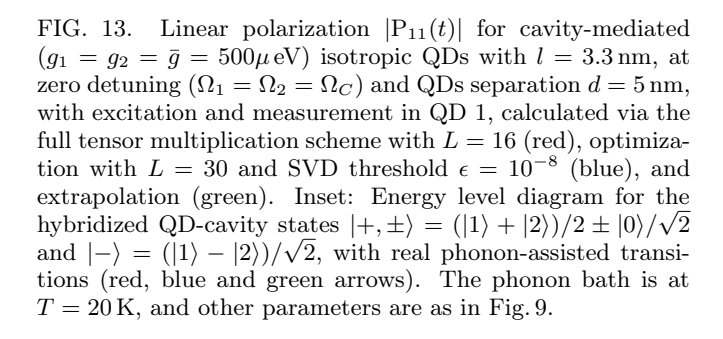


FIG. 12. Dephasing rates Γ_+ (blue) and Γ_- (red) of the hybridized states $|\pm\rangle$ at zero detuning as functions of the QD-cavity coupling strength g, calculated via the optimization scheme with extrapolation (solid lines), via FGR (dashed lines), and the most accurate calculation via the original tensor-multiplication scheme (crosses) for isotropic QDs with $l=3.3\,\mathrm{nm}$. The error of the extrapolation (dots) is shown on the left subplot. The right subplot further includes the virtual transitions on top of the real ones (dots). The phonon bath parameters are as in Fig. 9.

difference between the extrapolated and original calculations ($10^{-1} \,\mu\text{eV}$). This error is estimated by taking the final 4 data points of $\Gamma_{\pm}(L)$, performing the extrapolation with the last 3 points, and comparing the result with the extrapolation obtained using the first and last 2 points.

It is worth noting that the discrepancy between Fermi's golden rule (FGR) and the full calculation at large coupling strengths is due to virtual phonon-assisted transitions, not accounted for by the standard FGR calculation of real phonon-assisted transitions. The virtual transitions are significant compared to real transitions at such large coupling strengths [48, 49]. The virtual transitions can be taken into account by using the quadratic coupling model in [48] and added to the FGR result, or one can instead follow a combined approach [50]. Here we use the quadratic coupling model [48] to include real and virtual phonon-assisted transitions to second order. Details on FGR for real single phonon-assisted transitions and the refined model incorporating virtual transitions are provided in Appendix D. In Fig. 12, one can see that at large coupling strengths g (and thus large Rabi splittings R), the dephasing rates calculated via FGR for single real phonon-assisted transitions are exponentially small, approaches zero, despite the full calculation yielding finite values, whereas the modified calculation including virtual transitions shows a good agreement with the full extrapolated calculation. This agreement supports our conclusion on the origin of the decoherence in this regime and serves as a verification of the extrapolated results. The original data at such large coupling strengths begins to deviate significantly from the full calculation and the





refined approximation. Thus, the optimization scheme combined with extrapolation allowed us to demonstrate the physical mechanism of decoherence in a QD-cavity system in very strong coupling regime, which is understood and quantified in terms of virtual phonon-assisted transitions.

B. Necessity of the optimization in spatially extended systems

When the parts of a spatially extended quantum system interacts with the same environment, the memory time of the system can become very large and its quantum dynamics is difficult to capture accurately. As a typical example of this, we now consider Case 2, a system of two spatially separated QDs coupled to a microcavity and interacting with a shared phonon bath. Physically, the long memory times in this case are due to the shared bath, with coherent phonons travelling between the QDs, so the larger the dot separation, the larger the memory time.

Fig. 13 shows the linear polarization, $|P_{11}(t)|$, for a pair of cavity-mediated $(g_1 = g_2 = \bar{g} = 500\mu\,\text{eV})$ coupled isotropic QDs separated by a center-to-center distance $d=5\,\text{nm}$. In the case of zero detuning $(\Omega_1 = \Omega_2 = \Omega_C)$ and equal QD-cavity couplings $(g_1 = g_2)$, there are three resulting hybridized states, $|+,\pm\rangle = (|1\rangle+|2\rangle)/2\pm|0\rangle/\sqrt{2}$ and $|-\rangle = (|1\rangle - |2\rangle)/\sqrt{2}$, as depicted in the inset. Here $|1\rangle$ and $|2\rangle$ denote the exciton states in QD 1 and 2,

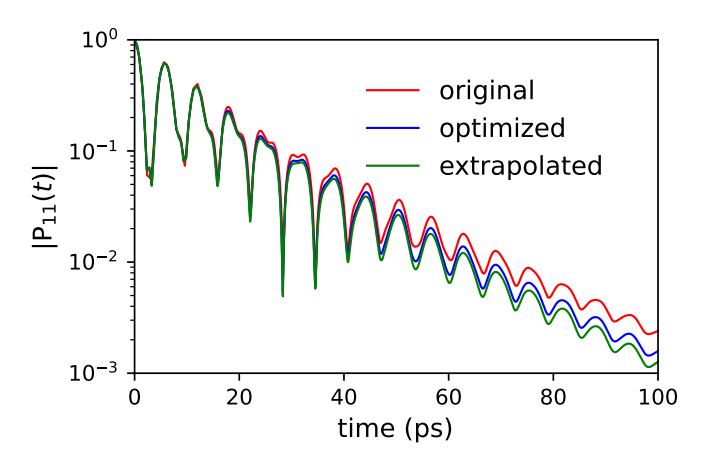


FIG. 14. As Fig. 13 but with the QD separation of $d = 45 \,\mathrm{nm}$.

respectively, and $|0\rangle$ is the cavity-photon state, see Appendix C and [29] for details. To generate the extrapolated data, a triexponential fit Eq. (19) is applied to $P_{11}(t)$ to extract the parameters corresponding to these hybridized states at different L and then extrapolate them to $L \to \infty$ using a power law fit similar to Eq. (20) and the procedure described in Sec. VI. The full extrapolated linear polarization is then found for any observation time t by adding $\Delta P_{11}(t) = P_{11}(t) - P_{11}^{\text{fit}}(t)$ to the triexponential form Eq. (19) used for the extrapolated parameters $C_i(\infty)$ and $\omega_i(\infty)$. Owing to the finite memory time, the difference $\Delta P_{11}(t)$ is independent of L, at least for a sufficiently large achievable L, and is found by subtracting from the full linear polarization $P_{11}(t)$, calculated at a finite L, its long-time dependence Eq. (19) with the extracted fit parameters $C_i(L)$ and $\omega_i(L)$. Fig. 13 compares the original, optimized, and extrapolated calculations, demonstrating a visual agreement between them. However, the separation of 5 nm is rather small and does not significantly increase the memory time, as detailed in Ref. [29]. We therefore observe a sufficient convergence of the original calculation, as in the QD-cavity system with small or moderate coupling g, see Figs. 9 and 11.

Fig. 14 shows the same quantity, but instead with a QD separation of $d=45\,\mathrm{nm}$, which displays a clear lack of convergence using the original method. Even the calculation using the optimization scheme is not very well converged, showing the necessity of the extrapolation. It should be noted that the extracted parameters do not follow a power-law convergence across all L values. Instead, the selected L values must be sufficiently high to enter the regime of power-law convergence. Due to this, the original technique in most regimes of spatially extended systems cannot generate enough data within the power-law convergence regime to provide an extrapolated calculation. Therefore, the optimized calculations are required for the extrapolation.

Fig. 15 shows the dephasing rates Γ_j extracted from the fit as functions of the QD separation d. The dephasing rates of the hybridized states $|+,\pm\rangle$ and $|-\rangle$ are

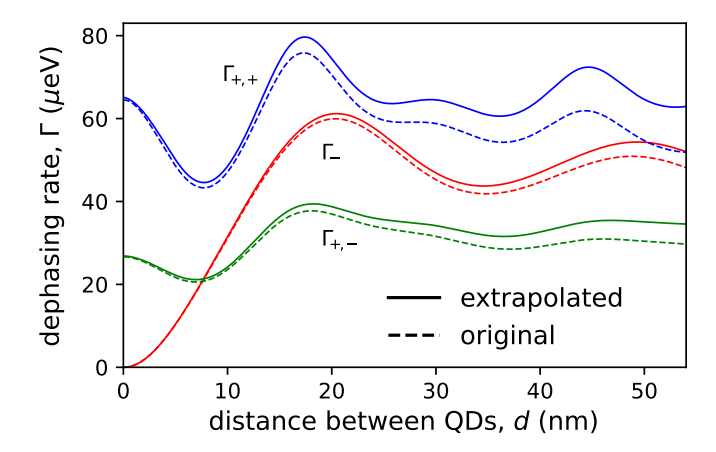


FIG. 15. Dephasing rates $\Gamma_{+,\pm}$ and Γ_{-} of the hybridized states as functions of d. Extrapolated rates (solid lines) are compared with the original rates with no optimization (dashed lines), for cavity-mediated coupled isotropic QDs with $l=3.3\,\mathrm{nm}$, interaction strength $g_1=g_2=\bar{g}=500\,\mu\mathrm{eV}$, and zero detuning. The phonon bath parameters are as in Fig. 13.

denoted by $\Gamma_{+,\pm}$ and Γ_{-} , respectively. As the QD separation increases, the memory time increases, and the original calculation gradually becomes increasingly inaccurate, requiring the optimization and extrapolation to accurately model the system.

VIII. CONCLUSION

In conclusion, we have developed a general optimization for path-integral tensor-multiplication schemes used to compute the exact non-Markovian dynamics in a large class of open quantum systems, with pair correlations and finite memory times. We demonstrate the optimization by investigating the linear polarization in quantum dot-cavity systems, and verify the scheme by comparison with the full original approach [21] and the TEMPO algorithm [34]. The optimized scheme has largely reduced memory storage requirements and approximately doubles the number of neighboring connections within the tensor network structure. Unlike other approaches, it provides a reliable dependence of the calculated quantum dynamics on the time step Δt of discretization, that allows us to reach Trotter's limit $\Delta t \to 0$ by extrapolation. This is crucial for systems with weak convergence to the exact solution. The increased number of neighbors paired with extrapolation gives access to previously inaccessible regimes, offering better convergence for systems with long memory times. We have considered two examples of such weak convergence in which the extrapolation allowed us to accurately calculate the quantum dynamics, revealing mechanisms of decoherence: QD-cavity in very strong coupling regime and cavity-mediated coupled qubits at large distances. For calculations already well converged

using traditional approaches, the optimization scheme offers greatly improved computational efficiency, shortening calculation times by up to two orders of magnitude.

ACKNOWLEDGMENTS

L.H. acknowledges support from the EPSRC under grant no. EP/T517951/1.

Appendix A: System Hamiltonians

In this work, we apply the optimization to two systems, referred to in the main text as Case 1: a QD-cavity system coupled to a bath of acoustic phonons, as detailed in [21], and Case 2: a QD-QD-cavity system coupled to the same acoustic phonon bath, as detailed in [29].

In Case 1, the full Hamiltonian has the form

$$H = H_0 + H_{\rm IB} \,, \tag{A1}$$

where

$$H_0 = \Omega_X d^{\dagger} d + \Omega_C a^{\dagger} a + g(d^{\dagger} a + a^{\dagger} d)$$
 (A2)

describes the coupling between the QD and the cavity, and $H_{\rm IB}$ is an independent boson (IB) model Hamiltonian describing the coupling of the QD to the environment. Here, d^{\dagger} is the fermionic exciton creation operator in the QD, a^{\dagger} is the cavity photon creation operator, Ω_X (Ω_C) is the exciton (cavity photon) energy, g is the coupling strengths between the QD and cavity. The IB model Hamiltonian describes the interaction of the QD exciton with an acoustic-phonon bath,

$$H_{\rm IB} = H_{\rm B} + H_{\rm int} \,, \tag{A3}$$

where

$$H_{\rm B} = \sum_{\mathbf{q}} \omega_{q} b_{\mathbf{q}}^{\dagger} b_{\mathbf{q}}$$
 and $H_{\rm int} = d^{\dagger} d \sum_{\mathbf{q}} \lambda_{\mathbf{q}} (b_{\mathbf{q}} + b_{-\mathbf{q}}^{\dagger})$
(A4)

are, respectively, the free phonon bath Hamiltonian and the QD coupling to the bath, where $b_{\bf q}^{\dagger}$ is the bosonic creation operator of a bulk phonon mode with the momentum ${\bf q}$ and frequency ω_q (denoting $q=|{\bf q}|$). The coupling of the exciton in the QD to the phonon mode ${\bf q}$ is given by the matrix element $\lambda_{\bf q}$, which depends on the material parameters and the QD exciton wave function. Its explicit form for isotropic QDs is provided in Appendix B.

In Case 2, for a system of two remote QDs coupled to an optical cavity, H_0 takes the form

$$H_0 = \Omega_1 d_1^{\dagger} d_1 + \Omega_2 d_2^{\dagger} d_2 + \Omega_C a^{\dagger} a + g_1 (d_1^{\dagger} a + a^{\dagger} d_1) + g_2 (d_2^{\dagger} a + a^{\dagger} d_2),$$
 (A5)

where d_j^{\dagger} is the fermionic exciton creation operator in QD j $(j = 1, 2), a^{\dagger}$ is the cavity photon creation operator, Ω_j

 (Ω_C) is the exciton (cavity photon) frequency, and g_j is the coupling strength between the exciton in QD j and the cavity photon. The generalized IB model Hamiltonian describes the interaction of the QD excitons with a shared acoustic-phonon bath,

$$H_{\rm IB} = H_{\rm B} + H_{\rm int} \,, \tag{A6}$$

where $H_{\rm B}$ is given in Eq. (A4) and

$$H_{\text{int}} = \sum_{j=1,2} d_j^{\dagger} d_j \sum_{\mathbf{q}} \lambda_{\mathbf{q},j} (b_{\mathbf{q}} + b_{-\mathbf{q}}^{\dagger})$$
 (A7)

is the coupling of the QD excitons to the bath, with $b_{\mathbf{q}}^{\dagger}$, \mathbf{q} , and ω_q defined above. It is convenient to write the interaction as

$$H_{\rm int} = d_1^{\dagger} d_1 V_1 + d_2^{\dagger} d_2 V_2 \,,$$
 (A8)

where

$$V_j = \sum_{\mathbf{q}} \lambda_{\mathbf{q},j} (b_{\mathbf{q}} + b_{-\mathbf{q}}^{\dagger}). \tag{A9}$$

The coupling of the exciton in QD j to the phonon mode \mathbf{q} is given by the matrix element $\lambda_{\mathbf{q},j}$ with its explicit form for isotropic QDs provided in Appendix B. For identical QDs separated by a distance vector \mathbf{d} , the matrix elements satisfy the relation

$$\lambda_{\mathbf{q},2} = e^{i\mathbf{q}\cdot\mathbf{d}}\lambda_{\mathbf{q},1} \,. \tag{A10}$$

Appendix B: Exciton-phonon coupling elements and phonon spectral density

Throughout this work, we use typical InGaAs QD parameters [48, 49], which are listed in the caption to Fig. 9. At low temperatures, the exciton-phonon interaction is primarily governed by the deformation potential coupling with longitudinal acoustic phonons. Assuming that the phonon parameters within the QDs closely resemble those of the surrounding material, and further assuming that the acoustic phonons exhibit linear dispersion, $\omega_q = v_s q$, where $q = |\mathbf{q}|$ and v_s is the sound velocity in the material, the exciton-phonon coupling matrix element for an exciton in QD j = 1, 2 is given by

$$\lambda_{\mathbf{q},j} = \frac{\sqrt{q} \, \mathcal{D}_j(\mathbf{q})}{\sqrt{2\rho_m v_s \mathcal{V}}},\tag{B1}$$

where ρ_m is the mass density of the material, V is the sample volume, and

$$\mathcal{D}_{j}(\mathbf{q}) = \int d\mathbf{r}_{e} \int d\mathbf{r}_{h} |\Psi_{X,j}(\mathbf{r}_{e}, \mathbf{r}_{h})|^{2} \left(D_{c} e^{i\mathbf{q} \cdot \mathbf{r}_{e}} - D_{v} e^{i\mathbf{q} \cdot \mathbf{r}_{h}} \right)$$
(B2)

is the coupling form-factor [48, 49], with D_c (D_v) being the deformation potential of the conduction (valence) band. Assuming a factorizable form of the exciton

wave functions, $\Psi_{X,j}(\mathbf{r}_e, \mathbf{r}_h) = \psi_{e,j}(\mathbf{r}_e)\psi_{h,j}(\mathbf{r}_h)$, where $\psi_{e(h),j}(\mathbf{r})$ is the confined electron (hole) ground state wave function in QD j, the form-factor simplifies to

$$\mathcal{D}_{j}(\mathbf{q}) = \int d\mathbf{r} \left[D_{c} |\psi_{e,j}(\mathbf{r})|^{2} - D_{v} |\psi_{h,j}(\mathbf{r})|^{2} \right] e^{i\mathbf{q}\cdot\mathbf{r}}.$$
 (B3)

Choosing spherically symmetric parabolic confinement potentials, the ground-state wave functions of the carriers take Gaussian form, which in the simpler case of equal electron and hole confinement lengths, $l_{e,j} = l_{h,j} = l_j$, is given by

$$\psi_{e,j}(\mathbf{r}) = \psi_{h,j}(\mathbf{r}) = \frac{1}{\pi^{3/4} l_j^{3/2}} \exp\left\{-\frac{(\mathbf{r} - \mathbf{d}_j)^2}{2l_j^2}\right\}, \quad (B4)$$

where \mathbf{d}_j is the coordinate of the center of QD j. Substituting Eq. (B4) into Eq. (B3), performing the integration over the whole space and using the result in Eq. (B1), we obtain

$$\lambda_{\mathbf{q},j} = \sqrt{q}\lambda_0 \exp\{-l_j^2 q^2/4\} e^{i\mathbf{q}\cdot\mathbf{d}_j}, \qquad (B5)$$

where

$$\lambda_0 = \frac{D_c - D_v}{\sqrt{2\rho_m v_s \mathcal{V}}}.$$
 (B6)

Choosing the first QD located at the origin $(\mathbf{d}_1 = 0)$ we find $\mathbf{d}_2 = \mathbf{d}$, where \mathbf{d} is the distance vector between the QDs. Converting the summation over \mathbf{q} to an integration, $\sum_{\mathbf{q}} \rightarrow \frac{\mathcal{V}}{(2\pi)^3} \int d\mathbf{q}$, and using spherical coordinates, we find the phonon spectral density

$$J_{jj'}(\omega) = J \,\omega^3 \exp\left\{-\frac{\omega^2 l^2}{v_s^2}\right\} \times \begin{cases} 1 & j = j'\\ \operatorname{sinc}\left(\frac{\omega d}{v_s}\right) & j \neq j', \end{cases}$$
(B7)

where

$$J = \frac{(D_c - D_v)^2}{4\pi^2 \rho_m v_s^5} \,, \tag{B8}$$

 $d = |\mathbf{d}|, \ l^2 = (l_j^2 + l_{j'}^2)/4$ (for brevity omitting the indices j and j' in the new length l introduced), and $\operatorname{sinc}(x) = \sin x/x$. However, in Case 1 only the j = j' case is required.

The spectral density $J_{jj'}(\omega)$ is used in Appendix C below for calculating the IB model cumulants.

Appendix C: Trotter's decomposition with linked cluster expansion

1. Trotter's decomposition

The time evolution operator Eq. (6) can be written in terms of two operators \hat{M} and \hat{W} , which describe the dynamics due to H_0 and $H_{\rm IB}$, respectively, each part being

analytically solvable. Using these operators, the dynamics without phonons over a single time step is described by \hat{M} , given by Eq. (7), and the exciton-phonon dynamics is given by

$$\hat{W}(t_n, t_{n-1}) = e^{iH_{\rm B}t_n} e^{-iH_{\rm IB}\Delta t} e^{-iH_{\rm B}t_{n-1}}, \qquad (C1)$$

where $t_n = n\Delta t$. Exploiting the commutativity of H_0 and H_B , one can write the time evolution operator Eq. (6) as

$$\hat{U}(t) = \mathcal{T} \prod_{n=1}^{N} \hat{W}(t_n, t_{n-1}) \hat{M}(t_n - t_{n-1}), \qquad (C2)$$

where \mathcal{T} is the time-ordering operator. Focusing on Case 2, we use the following basis states

$$|0\rangle = a^{\dagger} |VS\rangle$$
 and $|j\rangle = d_j^{\dagger} |VS\rangle$, (C3)

where $|\text{VS}\rangle$ represents the vacuum state of the QD-QD-cavity subsystem, and j=1, 2. \hat{W} and \hat{M} are both 3×3 matrices in the $|0\rangle, |1\rangle, |2\rangle$ basis, and due to the diagonal form of the exciton-phonon interaction, \hat{W} is diagonal. Its diagonal matrix elements can be written as

$$W_{i_n}(t_n, t_{n-1}) = \mathcal{T} \exp\left\{-i \int_{t_{n-1}}^{t_n} \tilde{V}_{i_n}(\tau) d\tau\right\}, \quad (C4)$$

where

$$\tilde{V}_{i_n}(\tau) = \xi_{i_n} V_1(\tau) + \eta_{i_n} V_2(\tau) \tag{C5}$$

for τ within the time interval $t_{n-1} \leq \tau \leq t_n$, with ξ_i and η_i being the components of the vectors

$$\vec{\xi} = \begin{pmatrix} 0 \\ 1 \\ 0 \end{pmatrix} \quad \text{and} \quad \vec{\eta} = \begin{pmatrix} 0 \\ 0 \\ 1 \end{pmatrix} , \tag{C6}$$

respectively, and $V_j(\tau) = e^{iH_{\rm B}\tau}V_je^{-iH_{\rm B}\tau}$ is the exciton-phonon coupling in the interaction representation, with V_j given by Eq. (A9). We use the indices i_n to indicate which state the system is in at a given time step n, being either $|0\rangle$, $|1\rangle$, or $|2\rangle$, with i_n taking the values 0, 1, or 2, respectively. The elements of the vectors $\vec{\xi}$ and $\vec{\eta}$ take care of the choice for which exciton is coupled to phonons at time step n. For example, if the system is in the first QD exciton state at time step n, then $i_n = 1$, and the exciton-phonon interaction V_1 occurs. Similarly, if $i_n = 0$, then both ξ and η are zero, since no exciton-phonon interaction occurs when the system is in the cavity state.

To find the polarization, we substitute the timeevolution operator $\hat{U}(t)$ in terms of the time ordered products of matrices \hat{W} and \hat{M} into Eq. (5). Then writing the matrix products explicitly yields

$$P_{jk}(t) = \sum_{i_{N-1}} \cdots \sum_{i_1} M_{i_N i_{N-1}} \dots M_{i_1 i_0} \times \langle W_{i_N}(t, t_{N-1}) \dots W_{i_1}(t_1, 0) \rangle_{\mathbf{B}}, \quad (C7)$$

where $i_0 = k$ and $i_N = j$ denote, respectively, the excitation mode k at t = 0 and measurement mode j is at the final time step $t_N = t$, and $M_{i_n i_m} = [\hat{M}(\Delta t)]_{i_n i_m}$. The W_{i_n} operators fully include the phonon contributions, therefore we separate this product from the rest of the expression in order to take the expectation value and apply the linked cluster theorem [41, 48, 49].

2. Linked cluster expansion

To calculate the expectation value of the products of the exciton-phonon interaction operators in Eq. (C7), we apply the linked cluster theorem. It allows us to write this expectation value as an exponential with a double sum over all possible second-order cumulants in the exponent [21, 41],

$$\langle W_{i_N}(t, t_{N-1}) \dots W_{i_1}(t_1, 0) \rangle_{\mathcal{B}} = \exp\left(\sum_{n=1}^N \sum_{m=1}^N \mathcal{K}_{i_n i_m}(|n-m|)\right)$$
(C8)

with the cumulants in Eq. (C8) given by

$$\mathcal{K}_{i_n i_m}(s) = -\frac{1}{2} \int_{t_{n-1}}^{t_n} d\tau_1 \int_{t_{m-1}}^{t_m} d\tau_2 \langle \mathcal{T} \tilde{V}_{i_n}(\tau_1) \tilde{V}_{i_m}(\tau_2) \rangle_{\mathcal{B}},$$
(C9)

where s = |n-m| and the double integration is performed over the time intervals $t_n - t_{n-1}$ and $t_m - t_{m-1}$. Using Eq. (C5), this cumulant can be expressed as

$$\mathcal{K}_{i_n i_m}(s) = \xi_{i_n} \xi_{i_m} K_{11}(s) + \eta_{i_n} \eta_{i_m} K_{22}(s)
+ (\xi_{i_n} \eta_{i_m} + \eta_{i_n} \xi_{i_m}) K_{12}(s), \quad (C10)$$

where we have introduced the cumulant elements

$$K_{jj'}(s) = -\frac{1}{2} \int_{t_{n-1}}^{t_n} d\tau_1 \int_{t_{m-1}}^{t_m} d\tau_2 D_{jj'}(\tau_1 - \tau_2), \quad (C11)$$

possessing the symmetry $K_{jj'}(s) = K_{j'j}(s)$. Here

$$D_{jj'}(t) = \int_0^\infty d\omega \ J_{jj'}(\omega) D(\omega, t) \,, \qquad \text{(C12)}$$

with

$$J_{jj'}(\omega) = \sum_{\mathbf{q}} \lambda_{\mathbf{q},j} \lambda_{\mathbf{q},j'}^* \delta(\omega - \omega_q), \qquad (C13)$$

and

$$D(\omega, t) = (\mathcal{N}_{\omega} + 1)e^{-i\omega|t|} + \mathcal{N}_{\omega}e^{i\omega|t|}$$
 (C14)

being, respectively the phonon spectral density and the standard phonon propagator, in which $\mathcal{N}_{\omega} = [e^{\omega/(k_BT)} - 1]^{-1}$ is the Bose distribution function, where T is the temperature, and k_B is the Boltzmann constant. The explicit analytical form of the spectral density $J_{jj'}(\omega)$ for isotropic QDs are derived in Appendix B.

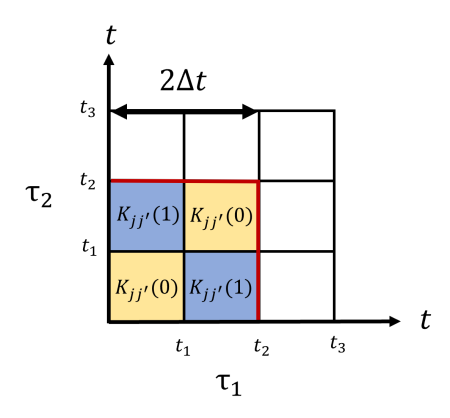


FIG. 16. A portion of the time grid up to $t = 2\Delta t$, illustrating Eq. (C18) that $C_{jj'}(2\Delta t)$ is composed of diagonal $K_{jj'}(s=0)$ (yellow) and off-diagonal contribution $K_{jj'}(s=1)$ (blue).

A convenient way to compute the cumulant elements Eq. (C11) is by defining the cumulant function

$$C_{jj'}(t) = -\frac{1}{2} \int_0^t d\tau_1 \int_0^t d\tau_2 D_{jj'}(\tau_1 - \tau_2) . \text{ (C15)}$$

Using the fact that $K_{jj'}(s)$ depends on the difference |n-m| only, and not on both time steps t_n and t_m individually every possible cumulant element across any time step can be computed recursively via

$$K_{jj'}(s) = \frac{1}{2} \left[C_{jj'} ((s+1)\Delta t) - (s+1)K_{jj'}(0) - 2\sum_{h=1}^{s-1} (s+1-h)K_{jj'}(h) \right],$$
(C16)

using

$$K_{ii'}(0) = C_{ii'}(\Delta t) \tag{C17}$$

as the initial value. Fig. 16 illustrates how Eq. (C15) can be used to express cumulant elements $K_{jj'}(s)$ as linear combinations of particular values of the cumulant function $C_{jj'}(t)$. For example, the cumulant element $K_{jj'}(1)$ can be computed using

$$C_{ii'}(2\Delta t) = 2K_{ii'}(0) + 2K_{ii'}(1)$$
. (C18)

One further note is that the cumulant elements $K_{12}(s)$ require contributions from $K_{12}(s=0)$, meaning that at time steps n and m, the system excitation is in both quantum dots. Physically, this never happens, but is introduced for mathematical consistency.

The linear polarization Eq. (C7) then takes the form

$$P_{jk}(t) = \sum_{i_{N-1}} \cdots \sum_{i_1} M_{i_N i_{N-1}} \dots M_{i_1 i_0}$$

$$\times \exp\left(\sum_{n=1}^{N} \sum_{m=1}^{N} \mathcal{K}_{i_n i_m}(s)\right). \tag{C19}$$

A particular realization or a path in the system evolution is indicated by the indices $i_{N-1}, \ldots, i_2, i_1$. However, to obtain the full quantum dynamics of the system, all possible realizations are to be summed over, meaning a summation over all of these indices, which is done in Eq. (C19). This is equivalent to the idea of path-integral approach.

3. Tensor multiplication scheme

The memory time of a system under consideration is discretized due to the application of Trotter's decomposition, and the number of discrete time steps within this memory time corresponds to the temporal correlations which are taken into account. The L-neighbor approach is then used to describe the temporal correlations between all considered steps within the memory time. The cumulant elements $K_{jj'}(s)$, with s = |n - m| increasing up to its maximum value, L, are found recursively from Eq.(C16).

By combining the contributions from matrices \hat{M} and the exponential term in Eq. (C19) describing the excitonphonon interactions across each time step, we define a quantity $F^{(s)}$ which is generated via the recursive relation

$$F_{pi_L...i_2}^{(s+1)} = \sum_{i_1=1,2,C} \mathcal{G}_{pi_L...i_1} F_{i_L...i_1}^{(s)}, \qquad (C20)$$

using $F_{i_L...i_1}^{(1)} = M_{i_1k}$ as the initial value, which is equivalent to Eq. (8), and $\mathcal G$ is the propagator given by Eq. (9).

Using the cumulant elements Eqs. (C10) and (C16) allows us to provide an explicit expression for the propagator Eq. (9) for $Case\ 2$:

$$\mathcal{G}_{pi_{L}...i_{2}i_{1}} = M_{i_{2}i_{1}} \exp \left\{ \xi_{i_{1}} \xi_{i_{1}} K_{11}(0) + \eta_{i_{1}} \eta_{i_{1}} K_{22}(0) + 2 \left(\xi_{i_{2}} \xi_{i_{1}} K_{11}(1) + \eta_{i_{2}} \eta_{i_{1}} K_{22}(1) \right) + 2 \left(\xi_{i_{2}} \eta_{i_{1}} + \eta_{i_{2}} \xi_{i_{1}} \right) K_{12}(1) + \dots + 2 \left(\xi_{p} \xi_{i_{1}} K_{11}(L) + \eta_{p} \eta_{i_{1}} K_{22}(L) \right) + 2 \left(\xi_{p} \eta_{i_{1}} + \eta_{p} \xi_{i_{1}} \right) K_{12}(L) \right\}$$
(C21)

with each element of the tensor corresponding to a particular realization of the system. Eq. (C21) reduces to a simpler form in $Case\ 1$ since there is no second QD and only the single QD is interacting with phonons. It is given by

$$\mathcal{G}_{pi_L...i_2i_1} = M_{i_2i_1} \exp\left\{\xi_{i_1}\xi_{i_1}K_{11}(0) + 2\xi_{i_2}\xi_{i_1}K_{11}(1) + \dots + 2\xi_{n}\xi_{i_1}K_{11}(L)\right\},$$
 (C22)

with i_n taking the values 0 or 1.

Appendix D: Real and virtual phonon-assisted transitions

FGR describes well the dephasing rates due to real phonon-assisted transitions. In the QD-cavity system

with only two hybridized polariton states $|\pm\rangle$, separated by the Rabi splitting R, the dephasing rates calculated via FGR are given by $\Gamma_{+}(R)$ and $\Gamma_{-}(R)$, respectively, for downward and upward transitions, see the inset in Fig. 11. Here

$$\Gamma_{-}(\omega) = \mathcal{N}_{\omega} \Gamma_{\rm ph}(\omega), \quad \Gamma_{+}(\omega) = (\mathcal{N}_{\omega} + 1) \Gamma_{\rm ph}(\omega), \quad (D1)$$

where \mathcal{N}_{ω} is the Bose function, and

$$\Gamma_{\rm ph}(\omega) = \frac{\pi}{4} \sum_{\mathbf{q}} |\lambda_{\mathbf{q},1}|^2 \, \delta(v_s q - \omega) \,,$$
 (D2)

calculated below for a spherical QD for zero detuning. The delta function in the above equation expresses the energy conservation in real transitions, indicating that the energy difference between the hybridized states should exactly match the energy of an emitted or absorbed phonon $\omega_q = v_s q$.

A refinement of the above FGR result used in this work is the inclusion of virtual phonon-assisted transitions to second order [48], so the dephasing rates of states $|\pm\rangle$ due to real and virtual transitions are given by

$$\bar{\Gamma}_{\pm}(R) = \Gamma_{\pm}(R) + \frac{4}{R^2} \int_0^{\infty} \frac{d\omega}{\pi} \, \Gamma_{+}(\omega) \, \Gamma_{-}(\omega) \,, \quad (D3)$$

where $\Gamma_{\pm}(\omega)$ are defined in Eq. (D1).

For an isotropic QD [21] in Case 1, $\Gamma_{\rm ph}(R)$ is calculated by integrating over the phonon degrees of freedom, and Eq. (D2) is further expressed as

$$\Gamma_{\rm ph}(R) = R^3 \frac{(D_c - D_v)^2}{16\pi \rho_m v_s^5} \exp\left\{-\frac{R^2 l^2}{v_s^2}\right\},$$
(D4)

with all the parameters defined in Appendix B.

For Case 2 with zero detuning, $\Gamma_{\rm ph}(\omega)$ takes the form

$$\Gamma_{\rm ph}(\omega) = \frac{\pi}{4} \sum_{\mathbf{q}} \left| (\lambda_{\mathbf{q},1} - \lambda_{\mathbf{q},2}) \right|^2 \delta(v_s q - \omega), \quad (D5)$$

where the rate $\Gamma_{\rm ph}(R)$, evaluated in [29], provides for an isotropic model of the QDs the explicit analytical result:

$$\Gamma_{\rm ph}(R) = \Gamma_0 \left(1 - \frac{\sin(Rd/v_s)}{Rd/v_s} \right) ,$$
 (D6)

where
$$\Gamma_0 = R^3 (D_c - D_v)^2 / (8\pi \rho_m v_s^5) e^{-l^2 R^2 / v_s^2}$$

- [1] H.-P. Breuer and F. Petruccione, *The Theory of Open Quantum Systems* (Oxford University Press, Oxford; New York, 2002).
- [2] I. De Vega and D. Alonso, Dynamics of non-Markovian open quantum systems, Rev. Mod. Phys. 89, 015001 (2017).
- [3] H.-P. Breuer, E.-M. Laine, J. Piilo, and B. Vacchini, Colloquium: Non-Markovian dynamics in open quantum systems, Rev. Mod. Phys. 88, 021002 (2016).
- [4] B. Krummheuer, V. M. Axt, and T. Kuhn, Theory of pure dephasing and the resulting absorption line shape in semiconductor quantum dots, Phys. Rev. B 65, 195313 (2002).
- [5] U. Hohenester, A. Laucht, M. Kaniber, N. Hauke, A. Neumann, A. Mohtashami, M. Seliger, M. Bichler, and J. J. Finley, Phonon-assisted transitions from quantum dot excitons to cavity photons, Phys. Rev. B 80, 201311 (2009).
- [6] E. Stock, M.-R. Dachner, T. Warming, A. Schliwa, A. Lochmann, A. Hoffmann, A. I. Toropov, A. K. Bakarov, I. A. Derebezov, M. Richter, V. A. Haisler, A. Knorr, and D. Bimberg, Acoustic and optical phonon scattering in a single In(Ga)As quantum dot, Phys. Rev. B 83, 041304 (2011).
- [7] D. E. Reiter, T. Kuhn, and V. M. Axt, Distinctive characteristics of carrier-phonon interactions in optically driven semiconductor quantum dots, Advances in Physics: X 4, 1655478 (2019).
- [8] P. Kaer, T. R. Nielsen, P. Lodahl, A.-P. Jauho, and J. Mørk, Non-Markovian Model of Photon-Assisted Dephasing by Electron-Phonon Interactions in a Coupled Quantum-Dot-Cavity System, Phys. Rev. Lett. 104,

- 157401 (2010).
- [9] A. Nazir and D. P. S. McCutcheon, Modelling excitonphonon interactions in optically driven quantum dots, J. Phys.: Condens. Matter 28, 103002 (2016).
- [10] S. Hughes, P. Yao, F. Milde, A. Knorr, D. Dalacu, K. Mnaymneh, V. Sazonova, P. J. Poole, G. C. Aers, J. Lapointe, R. Cheriton, and R. L. Williams, Influence of electron-acoustic phonon scattering on off-resonant cavity feeding within a strongly coupled quantum-dot cavity system, Phys. Rev. B 83, 165313 (2011).
- [11] A. Morreau, C. Joshi, and E. A. Muljarov, Phononinduced dephasing in quantum dot-cavity qed: Limitations of the polaron master equation (2020), arXiv:2002.01912 [cond-mat].
- [12] R. P. Feynman, A. R. Hibbs, and D. F. Styer, Quantum Mechanics and Path Integrals (Dover publ, Mineola, 2010).
- [13] D. E. Makarov and N. Makri, Path integrals for dissipative systems by tensor multiplication. Condensed phase quantum dynamics for arbitrarily long time, Chem. Phys. Lett. 221, 482 (1994).
- [14] N. Makri and D. E. Makarov, Tensor propagator for iterative quantum time evolution of reduced density matrices. I. Theory, J. Chem. Phys. 102, 4600 (1995).
- [15] N. Makri and D. E. Makarov, Tensor propagator for iterative quantum time evolution of reduced density matrices. II. Numerical methodology, J. Chem. Phys. 102, 4611 (1995).
- [16] N. Makri, Numerical path integral techniques for long time dynamics of quantum dissipative systems, J. Math. Phys. 36, 2430 (1995).
- [17] J. Shao and N. Makri, Iterative path integral calculation

- of quantum correlation functions for dissipative systems, Chem. Phys. **268**, 1 (2001).
- [18] J. Shao and N. Makri, Iterative path integral formulation of equilibrium correlation functions for quantum dissipative systems, J. Chem. Phys. 116, 507 (2002).
- [19] H. F. Trotter, On the product of semi-groups of operators, Proc. Am. Math. Soc. 10, 545 (1959).
- [20] M. Suzuki, Generalized trotter's formula and systematic approximants of exponential operators and inner derivations with applications to many-body problems, Comm. Math. Phys. 51, 183 (1976).
- [21] A. Morreau and E. A. Muljarov, Phonon-induced dephasing in quantum-dot-cavity QED, Phys. Rev. B 100, 115309 (2019).
- [22] E. Sim and N. Makri, Filtered propagator functional for iterative dynamics of quantum dissipative systems, Computer Physics Communications 99, 335 (1997).
- [23] E. Sim, Quantum dynamics for a system coupled to slow baths: On-the-fly filtered propagator method, J. Chem. Phys. 115, 4450 (2001).
- [24] R. Lambert and N. Makri, Memory propagator matrix for long-time dissipative charge transfer dynamics, Mol. Phys. 110, 1967 (2012).
- [25] L. Liu, J. Ren, and W. Fang, Improved Memory Truncation Scheme for Quasi-Adiabatic Propagator Path Integral via Influence Functional Renormalization (2024), arXiv:2406.01978 [physics].
- [26] N. Makri, Blip decomposition of the path integral: Exponential acceleration of real-time calculations on quantum dissipative systems, J. Chem. Phys. 141, 134117 (2014).
- [27] N. Makri, Iterative blip-summed path integral for quantum dynamics in strongly dissipative environments, J. Chem. Phys. 146, 134101 (2017).
- [28] D. Gribben, A. Strathearn, J. Iles-Smith, D. Kilda, A. Nazir, B. W. Lovett, and P. Kirton, Exact quantum dynamics in structured environments, Phys. Rev. Research 2, 013265 (2020).
- [29] L. M. J. Hall, L. S. Sirkina, A. Morreau, W. Langbein, and E. A. Muljarov, Controlling dephasing of coupled qubits via shared bath coherence, Phys. Rev. B 112, 045303 (2025).
- [30] A. M. Barth, A. Vagov, and V. M. Axt, Path integral description of combined Hamiltonian and non-Hamiltonian dynamics in quantum dissipative system, Phys. Rev. B 94, 125439 (2016).
- [31] M. Richter and B. P. Fingerhut, Coarse-grained representation of the quasi adiabatic propagator path integral for the treatment of non-Markovian long-time bath memory, J. Chem. Phys. 146, 214101 (2017).
- [32] V. Link, H.-H. Tu, and W. T. Strunz, Open Quantum System Dynamics from Infinite Tensor Network Contraction, Phys. Rev. Lett. 132, 200403 (2024).
- [33] A. Strathearn, P. Kirton, D. Kilda, J. Keeling, and B. W. Lovett, Efficient non-Markovian quantum dynamics using time-evolving matrix product operators, Nat. Comm. 9, 3322 (2018).
- [34] G. E. Fux, P. Fowler-Wright, J. Beckles, E. P. Butler, P. R. Eastham, D. Gribben, J. Keeling, D. Kilda, P. Kirton, E. D. C. Lawrence, B. W. Lovett, E. O'Neill, A. Strathearn, and R. de Wit, OQuPy: A Python package to efficiently simulate non-Markovian open quantum systems with process tensors, J. Chem. Phys. 161, 124108 (2024).
- [35] M. Richter and S. Hughes, Enhanced TEMPO algorithm

- for quantum path integrals with off-diagonal system-bath coupling: Applications to photonic quantum networks, Phys. Rev. Lett. **128**, 167403 (2022).
- [36] M. R. Jørgensen and F. A. Pollock, Exploiting the Causal Tensor Network Structure of Quantum Processes to Efficiently Simulate Non-Markovian Path Integrals, Phys. Rev. Lett. 123, 240602 (2019).
- [37] V. Link, H.-H. Tu, and W. T. Strunz, Open quantum system dynamics from infinite tensor network contraction, Phys. Rev. Lett. 132, 200403 (2024).
- [38] M. Cygorek and E. M. Gauger, ACE: A general-purpose non-Markovian open quantum systems simulation toolkit based on process tensors, J. Chem. Phys. 161, 074111 (2024).
- [39] L. S. Sirkina and E. A. Muljarov, Impact of the phonon environment on the nonlinear quantum-dot-cavity QED: Path-integral approach, Phys. Rev. B 108, 115312 (2023).
- [40] L. S. Sirkina, L. M. J. Hall, A. Morreau, W. Langbein, and E. A. Muljarov, Förster transfer between quantum dots in a shared phonon environment: A rigorous approach, revealing the role of pure dephasing (In Preparation).
- [41] G. D. Mahan, Many-Particle Physics (Springer US, Boston, MA, 2000).
- [42] A. W. Chin, J. Prior, R. Rosenbach, F. Caycedo-Soler, S. F. Huelga, and M. B. Plenio, The role of nonequilibrium vibrational structures in electronic coherence and recoherence in pigment-protein complexes, Nat. Phys. 9, 113 (2013).
- [43] M. D. Rey, A. W. Chin, S. F. Huelga, and M. B. Plenio, Exploiting Structured Environments for Efficient Energy Transfer: The Phonon Antenna Mechanism, J. Phys. Chem. Lett. 4, 903 (2013).
- [44] A. Blais, R.-S. Huang, A. Wallraff, S. M. Girvin, and R. J. Schoelkopf, Cavity quantum electrodynamics for superconducting electrical circuits: An architecture for quantum computation, Phys. Rev. A 69, 062320 (2004).
- [45] H. Zheng and H. U. Baranger, Persistent Quantum Beats and Long-Distance Entanglement from Waveguide-Mediated Interactions, Phys. Rev. Lett. 110, 113601 (2013).
- [46] I. Yeo, P.-L. De Assis, A. Gloppe, E. Dupont-Ferrier, P. Verlot, N. S. Malik, E. Dupuy, J. Claudon, J.-M. Gérard, A. Auffèves, G. Nogues, S. Seidelin, J.-P. Poizat, O. Arcizet, and M. Richard, Strain-mediated coupling in a quantum dot-mechanical oscillator hybrid system, Nat. Nanotechnol. 9, 106 (2014).
- [47] L. Childress, M. V. Gurudev Dutt, J. M. Taylor, A. S. Zibrov, F. Jelezko, J. Wrachtrup, P. R. Hemmer, and M. D. Lukin, Coherent Dynamics of Coupled Electron and Nuclear Spin Qubits in Diamond, Science 314, 281 (2006).
- [48] E. A. Muljarov and R. Zimmermann, Dephasing in Quantum Dots: Quadratic Coupling to Acoustic Phonons, Phys. Rev. Lett. 93, 237401 (2004).
- [49] E. A. Muljarov, T. Takagahara, and R. Zimmermann, Phonon-Induced Exciton Dephasing in Quantum Dot Molecules, Phys. Rev. Lett. 95, 177405 (2005).
- [50] E. A. Zibik, T. Grange, B. A. Carpenter, R. Ferreira, G. Bastard, N. Q. Vinh, P. J. Phillips, M. J. Steer, M. Hopkinson, J. W. Cockburn, M. S. Skolnick, and L. R. Wilson, Intersublevel polaron dephasing in self-assembled quantum dots, Phys. Rev. B 77, 041307 (2008).